ELSEVIER

Journal of Nuclear Materials 280 (2000) 235–245

journal of nuclear materials

www.elsevier.nl/locate/jnucmat

Effects of the accumulated annealing parameter on the corrosion characteristics of a Zr–0.5Nb–1.0Sn–0.5Fe–0.25Cr alloy

Jong Hyuk Baek [a,*], Yong Hwan Jeong [a], In Sup Kim [b]

[a] *Advanced Fuel Cladding Development, Korea Atomic Energy Research Institute, P.O. Box 105, Yusong, Taejon 305-600, South Korea*
[b] *Nuclear Engineering Department, Korea Advanced Institute of Science and Technology, P.O. Box 149, Yusong, Taejon 305-353, South Korea*

Received 24 May 1999; accepted 8 December 1999

Abstract

Corrosion behavior, hydrogen pickup, oxide microstructure, and precipitate characterization have been studied in order to investigate the effect of the accumulated annealing parameter on the corrosion characteristics in a Zr–Nb–Sn–Fe–Cr alloy. An autoclave corrosion test was carried out in 400°C steam for 300 days on the Zr–0.5Nb–1.0Sn–0.5Fe–0.25Cr alloy, which had been given 18 different accumulated annealing parameters. The corrosion rate increased with increasing the accumulated annealing parameter. To investigate the crystal structure of oxide layer, the corroded specimens were prepared to have an equal oxide thickness (~1.6 μm) by controlling exposure time. The relative fraction of tetragonal ZrO_2 also decreased gradually with increasing accumulated annealing parameter. From the hydrogen analysis of the corroded samples for 300 days, it was observed that, with increasing the size of precipitates, the hydrogen pickup was enhanced. It was revealed from transmission electron microscope (TEM) observation of the oxide that the larger precipitates still remained to be oxidized in the oxide layer and had undergone a reduction of Fe/Cr ratio from 2.1 to 1.5. The oxidation of the precipitates in the oxide gave rise to a volume expansion at the precipitate–oxide interface. This volume change could lead to the transformation in the oxide phase from tetragonal ZrO_2 to monoclinic ZrO_2 and in oxide structure from columnar grain to equiaxed grain. The precipitate in a Zr–0.5Nb–1.0Sn–0.5Fe–0.25Cr alloy is composed of Nb, Fe, and Cr and the Nb content in the precipitate increase with increasing accumulated annealing parameter. Thus, it can be thought that Nb within precipitates plays a key role in the microstructural change of oxide.

PACS: 28.41.T; 81.65.M; 81.40.E

1. Introduction

Modern nuclear power plants are required to operate under higher coolant temperature and higher pH conditions to increase the fuel burn-up and to extend the refueling cycle [1,2]. The major obstacle under these conditions has been found to be uniform corrosion of the Zircaloy cladding tubes caused by the growth of a uniform adherent oxide. At high oxide layer thickness, spalling of the oxide has occasionally been observed. In order to reduce the oxide growth, the development of new zirconium alloys with superior corrosion resistance to that of conventional Zircaloys has been required [3–7].

It is understood that the corrosion behavior of zirconium-based alloys is strongly influenced by the size and distribution of the second phase particles in the materials [8–14]. It was reported for Zircaloys that a coarse precipitate is beneficial for improving the resistance of uniform corrosion under PWR conditions, whereas a fine precipitate is beneficial for minimizing the nodular corrosion under BWR conditions [1,15,16]. The

* Corresponding author. Tel.: +82-42 868 8823; fax: +82-42 686 8346.
E-mail address: jhbaek@nanum.kaeri.re.kr (J.H. Baek).

0022-3115/00/$ - see front matter
PII: S0022-3115(99)00288-3

size and distribution of the precipitates are governed by thermomechanical treatments during the manufacturing process. During the last decades, the effect of heat treatment on the microstructure and the corrosion behaviors of Zircaloys cladding tubes have been extensively studied [17–21].

It is known that the addition of Nb in Zircaloys would improve the corrosion resistance and reduce the hydrogen pickup during the corrosion exposure [22–24]. Sabol et al., especially, reported that their alloy (Zr–1.0Nb–1.0Sn–0.1Fe, ZIRLO™) had the superior corrosion resistance to conventional Zircaloy-4 in 633 K water containing 70 and 210 ppm lithium as hydroxide and exhibited improved dimensional stability over Zircaloy-4 in reactor [25]. But there is insufficient schematic understanding of the effect of thermal treatment on the corrosion behavior of newly developed Nb-containing Zircaloy-type alloys.

It has been concluded that the corrosion resistance of Zircaloys can be related to the accumulated annealing parameter ($\sum A$) [15,17,19], which is an index of the total amount of heat treatment received in the α-region after the β-quenching. The parameter combines the annealing time (t) in hours and temperature (T) in Kelvin of each heat treatment. The accumulated annealing parameter ($\sum A$) can be described as follows:

$$\sum A = \sum_i t_i \exp[-Q/RT_i],$$

where Q is the activation energy and R is the gas constant.

In this study, the details of the relationship between the corrosion resistance and the accumulated annealing parameter are investigated and the results discussed in terms of the size and distribution of the second phase particles in a Zr–0.5Nb–1.0Sn–0.5Fe–0.25Cr alloy. Also the hydrogen pickup and the morphologies and structures of post-transition oxide after a 300-day-test in autoclave are assessed and discussed with the variations in the accumulated annealing parameter.

2. Experimental procedures

2.1. Specimens

The alloy was fabricated by arc remelting of nuclear purity sponge zirconium with high purity alloying elements in a water cooled copper hearth using a non-consumable tungsten electrode under an argon atmosphere. The chemical composition of the alloy used in this study is shown in Table 1. The button-type ingots were melted at least four times to ensure homogeneity of the alloying elements. After the solution treatment at 1050°C for 20 min, the ingots were water quenched to room temperature. Hot rolling by 70% reduction of thickness was performed after pre-heating to 700°C for 0.5 h. Cold rolling was repeated three times by 50% reduction of thickness per step to obtain 0.7 mm thick strips. Intermediate heat treatments were carried out in a vacuum of 1×10^{-5} Torr at various temperatures for 2 h and the final annealing was in the same atmosphere at 480°C for 3 h. The above-mentioned processes gave rise to 18 different values of the accumulated annealing parameter ($\sum A$) ranging from 7.7×10^{-19} to 5.3×10^{-17} h using $Q/R = 40\,000$ K. The sequence for the various accumulated annealing parameters is shown in Fig. 1.

Table 1
Chemical composition of Zr–Nb–Sn–Fe–Cr alloy (wt%)

Nb	Sn	Fe	Cr	O	Zr
0.53	0.97	0.50	0.26	0.12	Bal.

2.2. Corrosion tests

Specimens for the corrosion tests were machined to a size of $15 \times 20 \times 0.7$ mm^3. The coupons were mechanically ground with 800 Grid SiC paper and chemically polished using a pickling solution (a mixture of 5% HF, 45% HNO_3, and 50% H_2O) in the final step. Uniform corrosion tests were conducted in steam at a pressure of 10.3 MPa and temperature of 400°C for 300 days in a static autoclave, accordance to ASTM Practice for Aqueous Corrosion Testing of Samples of Zirconium and Zirconium Alloys Procedure (G2-88). The corrosion resistance was evaluated from weight gains after the corrosion tests.

2.3. Second phase particle analysis

Specimens with six kinds of the accumulated annealing parameters were selected for observation and identification of particles using a transmission electron microscope (TEM). Thin foil for the TEM was prepared at −45°C (applied voltage and current = 12 V/1.2 mA) by the twin-jet polishing with a solution of 10% $HClO_3$ and 90% C_2H_5OH after mechanical thinning to 70 μm. A TEM (JEOL 200 keV) equipped with energy dispersive X-ray spectroscopy (EDS) was used to observe and identify precipitates. More than 300 precipitates from each accumulated annealing parameter were analyzed to minimize the detection error. The mean size and area fraction of precipitates were measured using an image analyzer.

2.4. Observation of oxide crystal structure

The crystal structure of the oxide layer was characterized by a small angle XRD using an X-ray spectrometer (Rigaku, Rint 2500 XG) with a Cu-K_α source. The samples for XRD analysis were corroded in 400°C

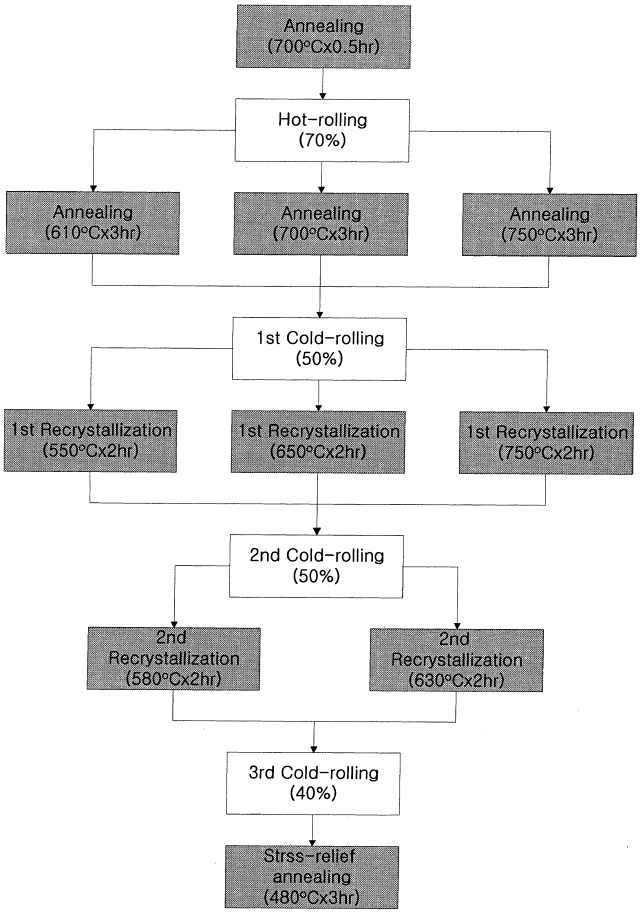

Fig. 1. Schematic sequence for the various accumulated annealing parameters.

steam for the different exposure time to have an equal thickness (≈1.6 μm) of oxide. Since the same manufacturing sequence except for annealing temperature applied to the samples, it can ignore the variations of peak intensity originated from different texture. Integrated intensities were calculated for various X-ray peaks, and the intensity of tetragonal ZrO_2 (1 0 1) peak was compared with that of the monoclinic ZrO_2 ($\bar{1}$ 1 1) peak. The ratio of integrated intensities was not equal to the amount of tetragonal ZrO_2 or monoclinic ZrO_2 directly, but the ratio showed a relative change in the crystal structure.

2.5. Hydrogen pickup

The hydrogen introduced during the 300-day-corrosion was measured using hot extraction and a hydrogen analyzer (LECO). This method gives a global hydrogen value (both metal and oxide) and does not measure the local concentration. The hydrogen pickup fraction was calculated based on the weight gain during the corrosion time.

2.6. Observation of oxide morphology

For the specimens corroded for 300 days, the oxide morphologies at the metal–oxide interface were observed using a scanning electron microscope (SEM, JEOL). The specimens were prepared using chemical etching of the metal with a solution of 10% HF, 45% HNO_3, and 45% H_2O.

TEM observations of the oxide layer at the interface were carried out using the above mentioned TEM on cross-sectional of thin films (i.e. with the observation plane perpendicular to the metal–oxide interface), which were prepared using an ion-milling machine.

3. Results

The effect of the accumulated annealing parameters on the weight gains at 400°C for 300 days (in post-transition regime) is shown in Fig. 2. This result illustrated that the weight gain increased with increasing

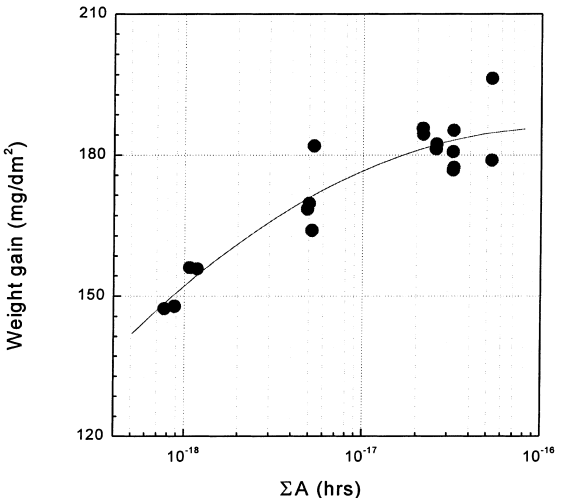

Fig. 2. Weight gain of samples corroded at 400°C for 300 days with accumulated annealing parameters.

accumulated annealing parameter. This result is contrary to that of Zircaloy-4 (Zr–1.5Sn–0.2Fe–0.1Cr) [15,18,19] but is consistent with that of Zircaloy-type alloys containing Nb studied by other researchers [16].

The accumulated annealing parameter is widely known to affect the size and number density of second phase particles in the matrix [15–19]. The size distribution of second phase particles in the matrix of the present alloy is shown in Fig. 3. Fig. 4 shows the influence of the accumulated annealing parameter on the mean equivalent diameter and the area fraction of second phase particles. As shown in Fig. 3, the mean equivalent sizes of the particles are correlated with the accumulated annealing parameter. The largest precipitate size of >750 nm existed when the accumulated annealing parameter was 5.3×10^{-17} h. As the accumulated annealing parameter increased from 7.7×10^{-19} to 5.3×10^{-17} h, the mean equivalent diameter and the area fraction of the precipitates increased simultaneously. Thus, it seems that the small precipitate sizes corresponded to high corrosion resistance and the large precipitate sizes to poor corrosion resistance. It follows that the corrosion resistance of this Zr–Sn–Fe–Cr alloy containing Nb can be enhanced by controlling the mean precipitate diameter to be <95 nm or to be as small as possible. The typical bright field images and EDS spectra of precipitates shown in Fig. 5 confirm that the mean size and number density of precipitates increased with increasing the accumulated annealing parameter from 7.7×10^{-19} to 5.3×10^{-17} h. As the precipitates grew, the content of Nb in the precipitate was more concentrated. The precipitates were round shaped and randomly distributed in grains or at grain boundaries for all $\sum A$. The precipitates in the alloy were mainly $ZrCr_2$ type Laves phase (C14, hcp) containing Zr, Nb, Fe and

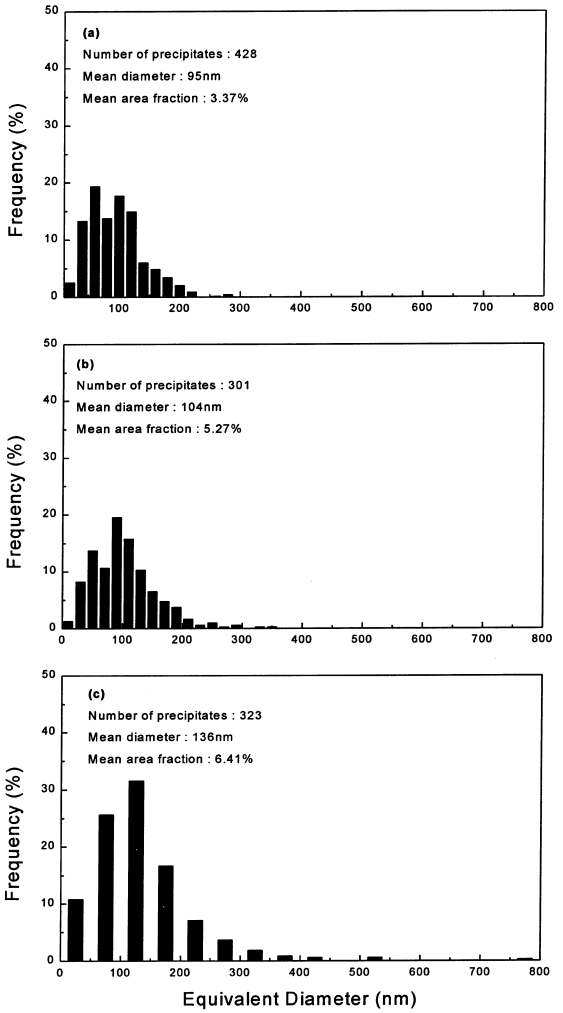

Fig. 3. Size distribution of second phase particles with accumulated annealing parameters: (a) 7.7×10^{-19} h; (b) 4.9×10^{-18} h; (c) 5.3×10^{-17} h.

Cr, in which the ratio of iron to chromium was about 2.1, in spite of the difference of accumulated annealing parameter.

For pre-transition oxides of equal thickness (1.6 μm), which were formed during the different exposure time, the relative amount of tetragonal ZrO_2 integrated over the total oxide thickness is plotted against the accumulated annealing parameter in Fig. 6. The good corrosion resistant samples having $\sum A < 1 \times 10^{-18}$ h exhibited a relative amount of more than 9% of tetragonal ZrO_2. When the accumulated annealing parameter increased to the range of 10^{-17} h order, the relative amount of tetragonal ZrO_2 was reduced to 6.6%. The oxide crystal structure in the pre-transition regime was thus influenced by the precipitate characteristics due to the variation of the accumulated annealing parameters.

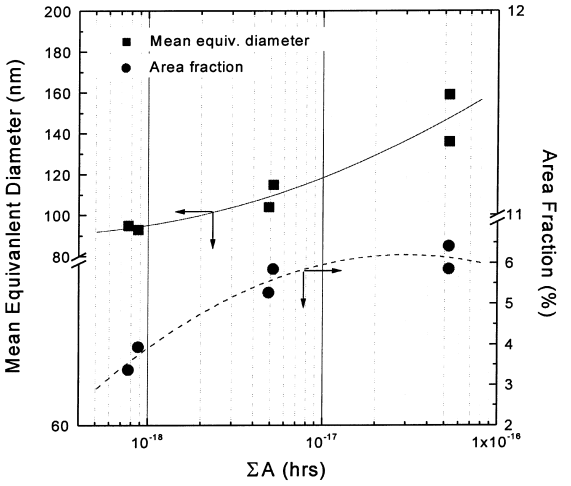

Fig. 4. Mean equivalent diameter and area fraction of second phase particles with accumulated annealing parameters.

After corroding in 400°C steam for 300 days, the hydrogen content of the corroded specimens was analyzed and the hydrogen pickup fraction was calculated. In Fig. 7, the hydrogen contents increased with increasing accumulated annealing parameter. The observed hydrogen content was 450 ppm at $\sum A = 7.7\times 10^{-19}$ h, and about 650 ppm at $\sum A = 5.3 \times 10^{-17}$ h. The hydrogen pickup fraction also slightly increased as the accumulated annealing parameter increased. The resultant accelerated the corrosion rate of the specimens having larger precipitates also resulted in an increase of the observed hydrogen content.

The SEM morphologies of the oxide beneath the metal–oxide interface in the 300-day-specimens were shown in Fig. 8. In the case of $\sum A = 7.7 \times 10^{-19}$ h (Fig. 8(a)), the interface mostly showed protruded round oxide. In comparison, Fig. 8(b) with $\sum A = 5.3 \times 10^{-17}$ h showed protruded round oxide with large lumps. The difference of oxide morphology basically resulted from the variation of the accumulated annealing parameter. The corrosion rate of specimens having larger protruded lumps was faster than that having smaller lumps.

TEM micrographs of the oxide beneath the metal–oxide interface were shown in Fig. 9. The morphology of oxide, within about 160 nm from the metal–oxide interface, having the lower accumulated annealing parameter of $\sum A = 7.7 \times 10^{-19}$ h was mainly a columnar structure, and the incorporated precipitates could not easily detected in the oxide because of small size of precipitates. In the intermediate and outer oxides, the oxide structures were changed from columnar-type shape to equiaxed-type shape. In the case of higher accumulated annealing parameter ($\sum A = 5.3 \times 10^{-17}$ h), however, the incorporated precipitates were easily observed in the oxide beneath the interface and their surroundings appeared to have an equiaxed structure. The ratio of iron to chromium of the incorporated precipitates was less than 1.5 in comparison with 2.1 before oxidation. The oxide structures at the surroundings near the oxidizing precipitate exhibited the fragmented (or equiaxed) structures but the columnar structures were still observed at oxide region far from the precipitate. The diffraction pattern, as shown in top-left of Fig. 9(b), at the boundary area between incorporated precipitate and oxide was a ring type in contrast to that of the oxide in bottom-right of Fig. 9(b). From the ring-type pattern, the nanocrystallized structure, in which the size of precipitates was very fine ($\leqslant 10$ nm), would be developed at the boundary of the incorporated precipitates in the oxide.

4. Discussions

It was shown in Fig. 2 that the corrosion resistance of this Nb-containing Zr–Sn–Fe–Cr alloy was improved by decreasing the accumulated annealing parameter to less than 1×10^{-18} h. As mentioned in Fig. 7, the control of the accumulated annealing parameter to be less than 1×10^{-18} h gave an advantage from the viewpoint of hydrogen pickup during the 300-day-corrosion test. That is, the samples having the good corrosion resistance showed the lowest hydrogen pickup. In addition to the influence of hydrogen pickup, the accumulated annealing parameter affected the mean size and distribution of the second phase particles in the matrix. As the accumulated annealing parameter increased, the mean size and area fraction of precipitates consistently increased. In general, it is known that the hydrogen contents in the metal of zirconium alloy may be affected by the corrosion rate [16,25]. The increase in the size and area fraction of the precipitates resulted in increased pickup of hydrogen, which was introduced during the corrosion reaction. The reason is that precipitates have greater affinity for hydrogen than the matrix [9]. If the size and the number density of precipitates were large then the hydrogen ion could easily be diffuse via the precipitates to the metal–oxide interface, where the oxidation reaction was occurring. This illustrates why the higher accumulated annealing parameter enhanced slightly hydrogen pickup fraction in the matrix during the corrosion test.

Jeong et al. reported the corrosion rate of Zircaloy-4 in LiOH aqueous solution affected on the morphology of oxide beneath the metal–oxide interface [26,27]. The change of oxide morphologies at the interface between the oxide and metal occurred with varying accumulated annealing parameter. In the case of the higher accumulated annealing parameter with 5.3×10^{-17} h, the oxide morphologies at the interface appeared to be a protruded shape with larger lumps. It is thought that the

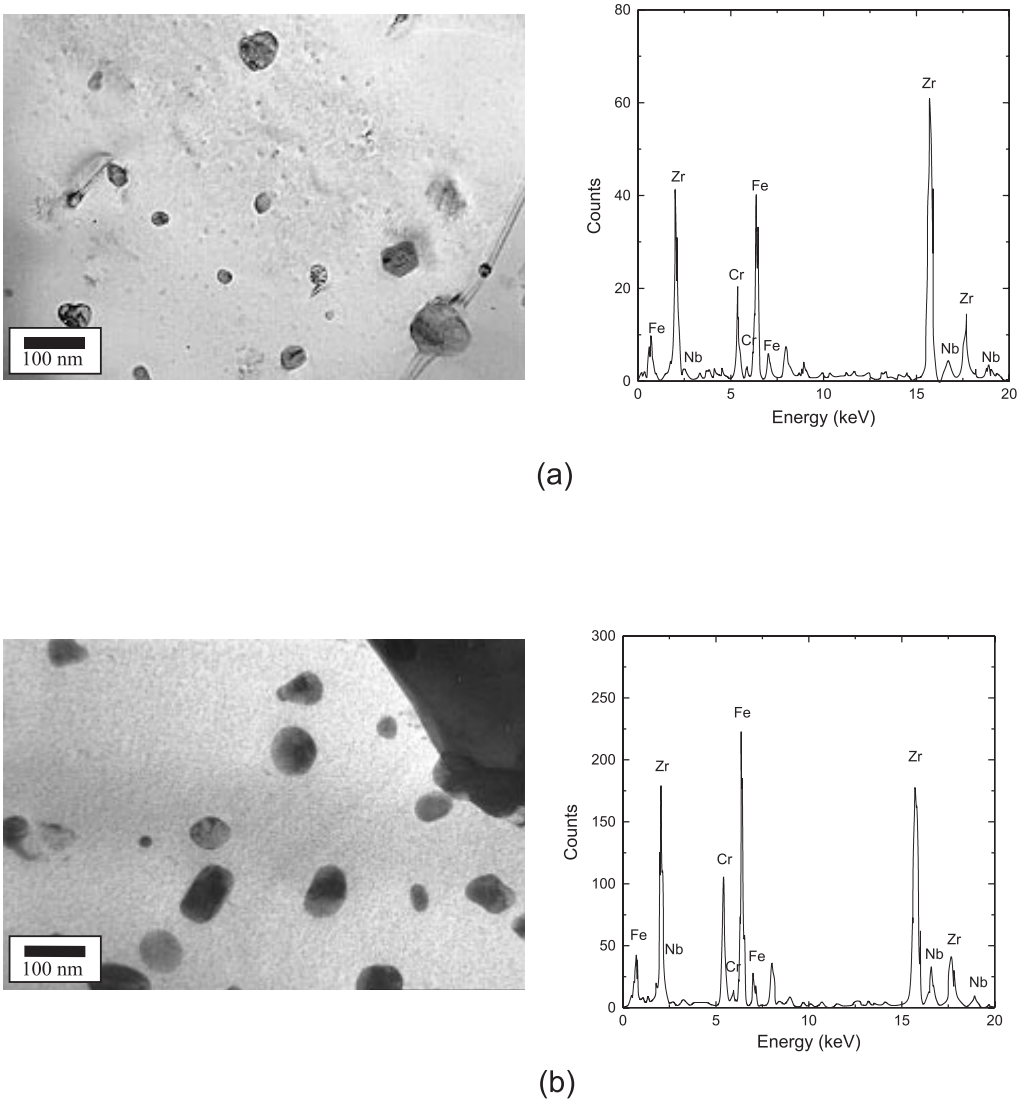

Fig. 5. TEM images and EDS spectra of second phase particles: (a) 7.7×10^{-19} h; (b) 5.3×10^{-17} h.

growth of oxide lumps resulted from the high corrosion rate. It is suggested that this morphological change is influenced by the different size of second phase particles.

Many researchers have proposed that the oxide transformed from the tetragonal ZrO_2 structure to the monoclinic ZrO_2 structure in the oxidation process of zirconium-based alloys [14,28–31]. It has been understood that the tetragonal ZrO_2 would be generated in a high compressive stress field beneath the metal–oxide interface and acted as barrier layer to reduce the corrosion rate [32–34]. It was shown in Fig. 6 that the relative amount of tetragonal ZrO_2 for an equal thickness of pre-transition oxide decreased drastically as the accumulated annealing parameter increased. When the relative amount of tetragonal ZrO_2 was more than 9%, the corrosion rate of this Nb-containing Zr–Sn–Fe–Cr alloy was retarded. From the strong dependence between the precipitates and the accumulated annealing parameter, the relative amount of tetragonal ZrO_2 was affected by the changes of precipitates in the matrix. It is important that the transformation of the oxide structure from tetragonal ZrO_2 to monoclinic ZrO_2 was delayed in samples having a smaller size of precipitates in pre-transition oxides. The slow transformation from tetragonal ZrO_2 to monoclinic ZrO_2 gave an advantage of the corrosion resistance of this alloy at low $\sum A$.

The TEM observation, Fig. 9, showed that the detectability of incorporated precipitates in the oxide is dependent on the accumulated annealing parameter. At high accumulated annealing parameter (5.3×10^{-17} h),

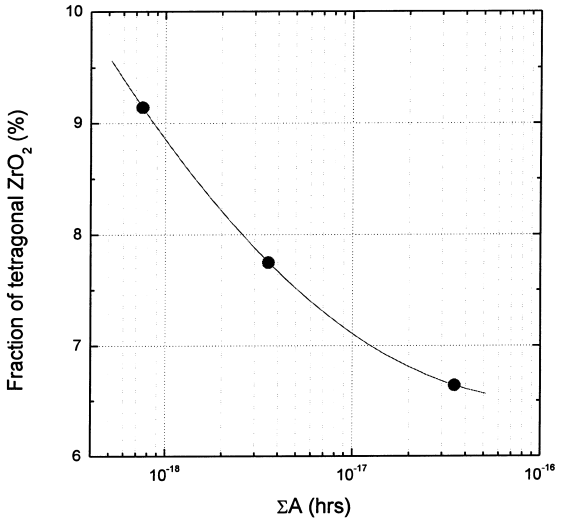

Fig. 6. Relative fraction of tetragonal ZrO_2 in oxide of equal thickness with accumulated annealing parameters.

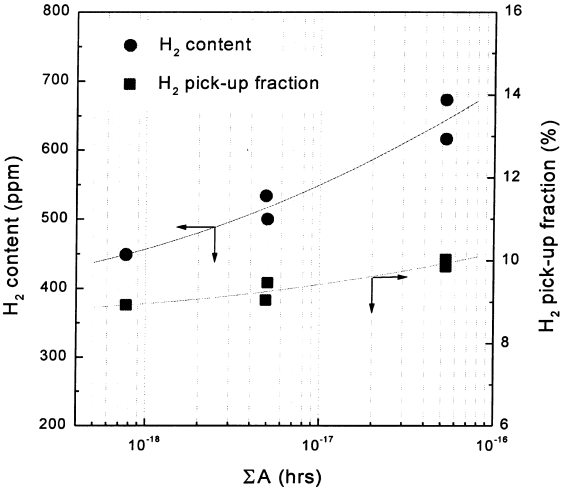

Fig. 7. The content and pick-up fraction of hydrogen with accumulated parameters after corroding at 400°C for 300 days.

equiaxed oxide structures present at the surrounds of incorporated precipitate in the oxide. The equiaxed oxide resulted from high corrosion rate in materials with the higher accumulated annealing parameter.

When a large precipitate is incorporated in the oxide, the precipitate might exist unoxidised at the early stage of corrosion because of the different corrosion rate between the matrix and the precipitate. As the corrosion reaction progresses, the peripheries of the incorporated precipitate would preferentially be corroded. The iron in the incorporated precipitate would rapidly diffuse out because of the larger diffusion coefficient of iron than other elements in the precipitate [35]. This is why the

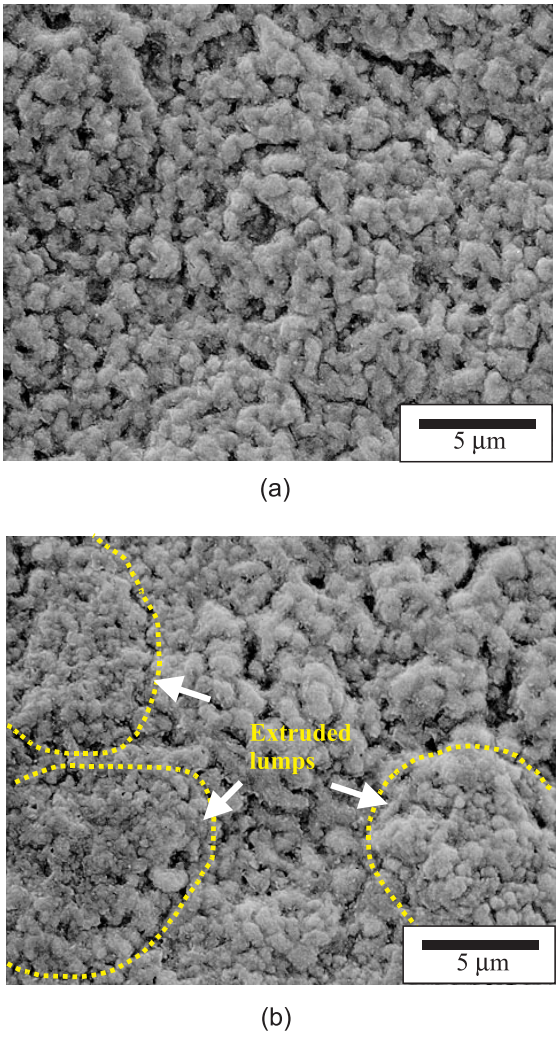

Fig. 8. SEM morphologies of oxide beneath metal–oxide interface: (a) 7.7×10^{-19} h; (b) 5.3×10^{-17} h.

iron to chromium ratio in the incorporated precipitates is lower than that in the matrix precipitates. The nanocrystallized structure of the incorporated precipitate caused the ring-type diffraction pattern in Fig. 9(b). The schematic diagrams of the TEM oxide morphologies with accumulated annealing parameter are shown in Fig. 10. When the accumulated annealing parameter increased, the size and number of the incorporated precipitates also increased but the region of columnar structure decreased.

Fig. 11 illustrates the role of the incorporated Nb-containing precipitates in the oxide layer. When a precipitate is incorporated into the columnar oxide, the peripheries of the incorporated precipitate would preferentially start to oxidize due to the out-diffusion of the alloying elements like iron, chromium, and niobium. The oxidation of alloying elements at a metal–oxide

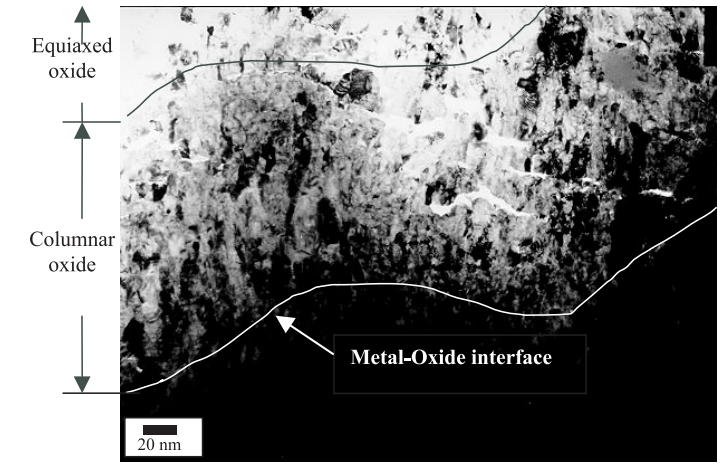

(a)

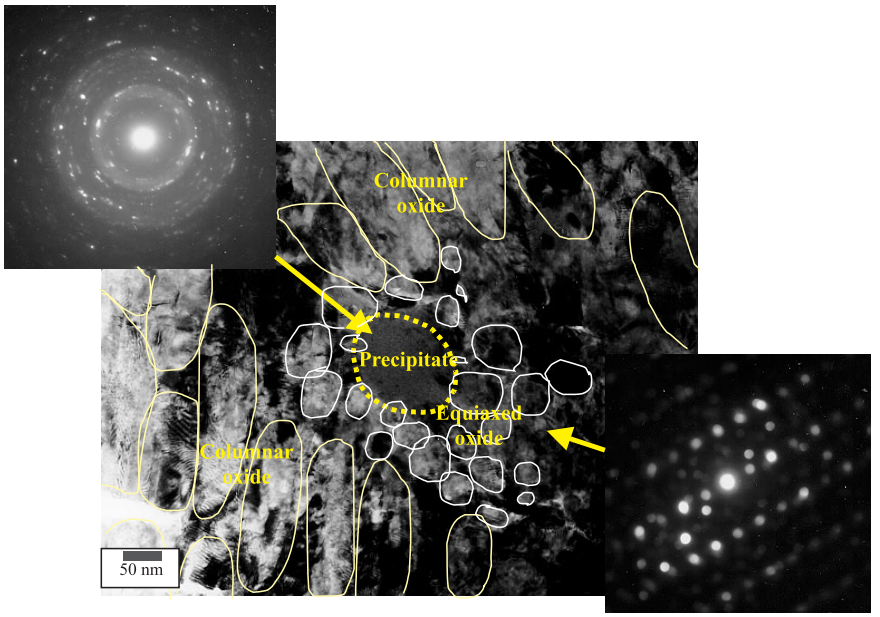

(b)

Fig. 9. TEM morphologies and incorporated precipitates of oxide beneath metal–oxide interface: (a) 7.7×10^{-19} h; (b) 5.3×10^{-17} h.

interface would locally cause the volume expansion of that region due to the Pilling–Bedworth ratio. The tensile stress due to the volume expansion would compensate the compressive stress that stabilizes the columnar structure. The process would favor a nanocrystallized structure at the peripheries of the incorporated precipitate. This explains why the oxide at the surroundings of the precipitate transform from the columnar structure to an equiaxed structure. As the diffusing out of the alloying elements from the incorporated precipitates continued, the columnar region would be decreased. The equiaxed oxide structure would provide a shorter diffusion path of the oxygen ion. The large precipitates resulting from a high accumulated annealing parameter can thus accelerate the corrosion process of this Nb-containing Zr–Sn–Fe–Cr alloy.

Briefly, the corrosion resistance of this Nb-containing Zr–Sn–Fe–Cr alloy was improved as the $\sum A$ or the precipitate size decreased. Also the relative fraction of tetragonal ZrO_2 for equal oxide thickness decreased with increasing the accumulated annealing parameter. These results are contrary to those of previous works for

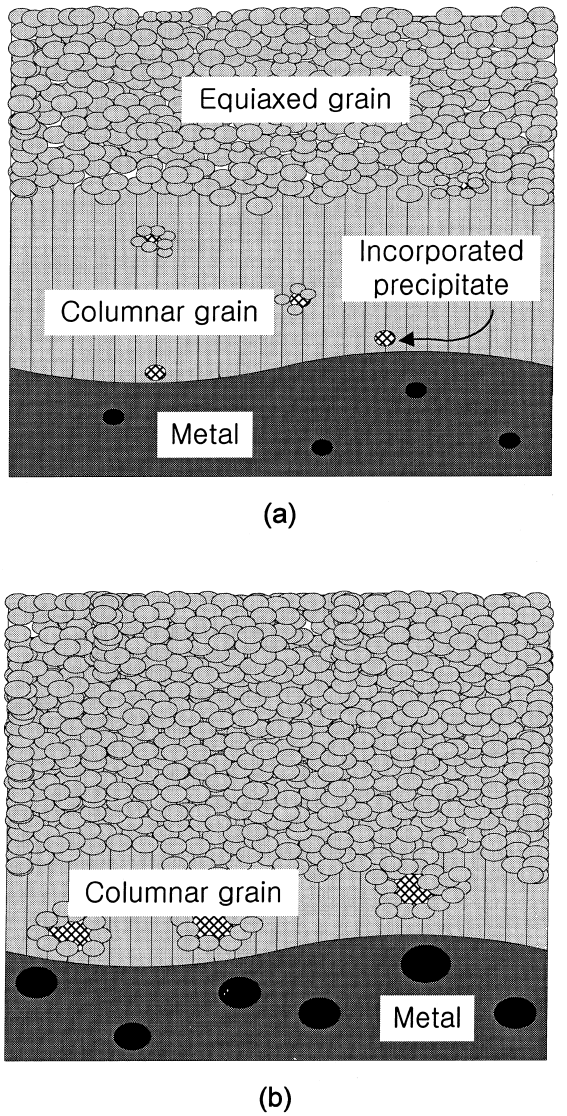

Fig. 10. Schematic diagrams with accumulated annealing parameters of oxide beneath metal–oxide interface: (a) 7.7×10^{-19} h; (b) 5.3×10^{-17} h.

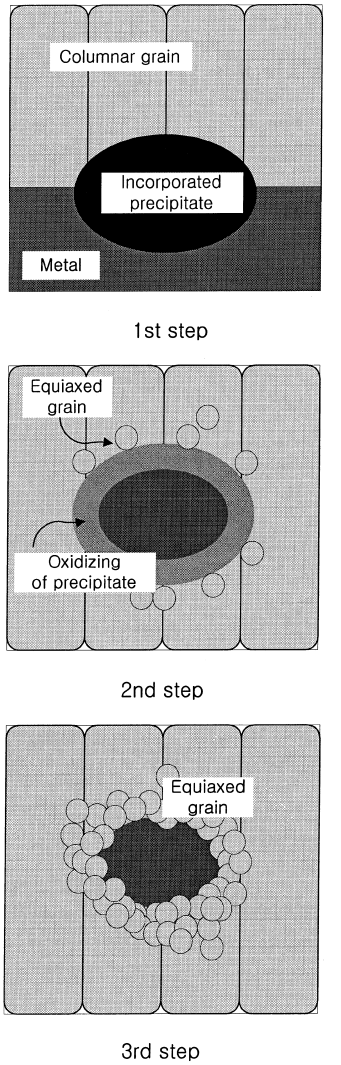

Fig. 11. Schematic diagram for the role of the Nb-containing second phase particles.

Zircaloy-4 [1,15]. That is, the corrosion resistance of Zircaloy-4 in PWR was improved as the $\sum A$ increased. Thus the mean size of precipitates was to be larger than 0.09 mm to improve corrosion properties in reactor.

Godlewski investigated the fraction of tetragonal ZrO_2 in oxide layer of Zircaloy-4 using XRD and Raman spectroscopy with varying the exposure time and the distance from metal–oxide interface [31]. He reported that the corrosion rate and transition of the corrosion rate were closely related with the fraction of tetragonal ZrO_2 in oxide. He pointed that the fraction of tetragonal ZrO_2 in oxide increased slightly because of generation of compressive stress field during the precipitates oxidation. At transition, the fraction of tetragonal ZrO_2 decrease drastically and then increased again due to the oxidation of another precipitates. But he did not observe the oxidation process of precipitates in oxide using TEM. Pecheur et al. reported that the segregation of Fe and Cr in precipitates stabilized the tetragonal ZrO_2 phase because of delayed oxidation of alloying elements such as Fe and Cr with respect to zirconium in precipitates [36]. They said that the nanocrystallization in the peripheries of precipitates was corresponded to the existence of tetragonal ZrO_2 phase in oxide.

However, the proposals of Godlewski and Pecheur et al. for effects of precipitates on corrosion mechanism

of Zircaloy-4 cannot interpret the results of this Nb-containing Zr–Sn–Fe–Cr alloy. By the way, another results by Isobe et al., who evaluated the corrosion resistance and hydrogen pickup of the VAZ alloys (Zr–Nb–Fe–Cr–optional Mo) for various $\sum A$, are consistent with this result [16]. The corrosion resistance of VAZ alloy decreased as the $\sum A$ increased. But they left all the whys unanswered.

It can be thought from the different point of view that the decrease of corrosion resistance in this Nb-containing Zr–Sn–Fe–Cr alloy occurred as the $\sum A$ increased. First of all, the chemical composition of precipitates in a Nb-containing Zr–Sn–Fe–Cr alloy is different from that of Zircaloy-4. The composition in precipitates is composed of Zr, Nb, Fe, and Cr for this alloy, while Zr, Fe, and Cr for Zircaloy-4. It can be supposed that the roles of Nb-containing precipitates be different from those without Nb. In other words, the Nb-containing precipitates of this Zr–0.5Nb–1.0Sn–0.5Fe–0.25Cr alloy would relax the high compressive stress fields at surroundings of the precipitates in oxide layer. This results in the oxide transformation from columnar structure to equiaxed structure at surroundings of the oxidizing precipitates. This hypothesis is supported from the decrease of relative tetragonal ZrO_2 phase in samples of larger precipitates and the observation of equaixed structures at surroundings of oxidizing precipitates in the oxide layer. Thus, the Nb within precipitates plays a key role in microstructural change in oxide layer. The higher concentration of Nb in precipitates having higher $\sum A$, especially, is very important for the oxide transformation from the tetragonal ZrO_2 phases to the monoclinic ZrO_2 phases or from the columnar oxide structures to the equiaxed oxide structures. Another possibility for the reasons of increasing corrosion rate with the $\sum A$ is the change of relative tetragonal ZrO_2 due to the alteration of Nb concentration within α-Zr matrix. However, it is unclear in this study how Nb in Nb in precipitates and matrix induce the microstructural change of oxide, so the extended works for revealing the reasons shall be performed in detail.

5. Conclusions

The corrosion resistance of a Zr–0.5Nb–1.0Sn–0.5Fe–0.25Cr alloy was improved by decreasing the accumulated annealing parameter to less than 1×10^{-18} h. There was also a strong correlation between the size and area fraction of second phase particles and the accumulated annealing parameter, which also affected on the amount of tetragonal ZrO_2 in the pre-transition oxide layer. That is, the larger precipitates enhanced the transformation from the tetragonal ZrO_2 structure to the monoclinic structure in the pre-transition oxide, and the corrosion rate of the alloy increased with decreasing amount of the tetragonal oxide layer.

After the 300-day-corrosion tests, the content of hydrogen increased slightly as the accumulated annealing parameter increased. SEM observations illustrated that the larger precipitates made the oxide morphologies beneath the metal–oxide interface to have into a more lumped shape. From TEM examinations, the incorporation of larger precipitates into the oxide enhanced the transformation of the columnar oxide structure to an equiaxed oxide structure. This resulted in an acceleration of the corrosion rate due to shortening the path of the oxygen ion to the metal–oxide interface via the oxide layer. It is concluded that controlling the precipitates to be <95 nm in mean size leads to an advantage for improving corrosion resistance in this Nb-containing Zr–Sn–Fe–Cr alloy.

Acknowledgements

This project has been carried out under the Nuclear R&D Program by MOST.

References

[1] F. Garzarolli, H. Stehle, E. Steinberg, in: E.D. Bradley, G.P. Sabol, (Eds.), Zirconium in the Nuclear Industry: 11th International Symposium, ASTM STP 1295, American Society for Testing and Materials, 1996, p. 12.

[2] A.M. Garde, S.R. Pati, M.A. Krammen, G.P. Smith, R.K. Endter, in: A.M. Garde, E.D. Bradley (Eds.), Zirconium in the Nuclear Industry: 10th International Symposium, ASTM STP 1245, American Society for Testing and Materials, 1994, p. 760.

[3] G.P. Sabol, G.P. Klip, M.G. Balfour, E. Roberts, in: L.F.P. Van Swam, C.M. Eucken (Eds.), Zirconium in the Nuclear Industry: Eighth International Symposium, ASTM STP 1023, American Society for Testing and Materials, 1989, p. 227.

[4] T. Isobe, Y. Matsuo, in: C.M. Eucken, A.M. Garde (Eds.), Zirconium in the Nuclear Industry: Ninth International Symposium, ASTM STP 1132, American Society for Testing and Materials, 1991, p. 346.

[5] M. Harada, M. Kimpara, K. Abe, in: C.M. Eucken, A.M. Garde (Eds.), Zirconium in the Nuclear Industry: Ninth International Symposium, ASTM STP 1132, American Society for Testing and Materials, 1991, p. 368.

[6] Y. Etoh, S. Shimada, T. Yasuda, T. Ikeda, R.B. Adamson, J.-S. Fred Chen, Y. Ishii, K. Takai, in: E.D. Bradley, G.P. Sabol (Eds.), Zirconium in the Nuclear Industry: 11th International Symposium, ASTM STP 1295, American Society for Testing and Materials, 1996, p. 825.

[7] A.V. Nikulina, V.A. Markelov, M.M. Pregud, Y.K. Bibilashvili, V.A. Kotrekhov, A.F. Lositsky, N.V. Kuzmenko, Y.P. Shevnin, V.K. Shamardin, G.P. Kobylyansky, A.E. Novoselov, in: E.D. Bradley, G.P. Sabol (Eds.), Zirconium in the Nuclear Industry: 11th International Symposium, ASTM STP 1295, American Society for Testing and Materials, 1996, p. 785.

[8] R.M. Kruger, R.B. Adamson, S.S. Brenner, J. Nucl. Mater. 189 (1992) 193.
[9] Y. Hatano, K. Isobe, R. Hitaka, M. Sugisaki, J. Nucl. Sci. Technol. 33 (12) (1996) 944.
[10] O.T. Woo, J.C. Capenter, J.A. Sawuchu, S.K. Macewen, J. Nucl. Mater. 172 (1990) 71.
[11] X. Meng, D.O. Northwood, in: L.F.P. Van Swam, C.M. Eucken (Eds.), Zirconium in the Nuclear Industry: Eighth International Symposium, ASTM STP 1023, American Society for Testing and Materials, 1989, p. 478.
[12] Th. Andersson, G. Vesterlund, in: D.G. Franklin (Ed.), Zirconium in the Nuclear Industry: Fifth International Symposium, ASTM STP 754, American Society for Testing and Materials, 1982, p. 75.
[13] J.P. Poster, J. Dougherty, M.G. Burke, J.F. Bates, S. Worcester, J. Nucl. Mater. 173 (1990) 164.
[14] H. Anada, B.J. Herb, K. Nomoto, S. Hagi, R.A. Graham, T. Kuroda, in: E.D. Bradley, G.P. Sabol (Eds.), Zirconium in the Nuclear Industry: 11th International Symposium, ASTM STP 1295, American Society for Testing and Materials, 1996, p. 74.
[15] G. Garzarrolli, E. Steinberg, H.G. Weidinger, in: L.F.P. Van Swam, C.M. Eucken (Eds.), Zirconium in the Nuclear Industry: Eighth International Symposium, ASTM STP 1023, American Society for Testing and Materials, 1989, p. 202.
[16] T. Isobe, T. Matsuo, Y. Mae, in: A.M. Garde, E.D. Bradley (Eds.), Zirconium in the Nuclear Industry: Tenth International Symposium, ASTM STP 1245, American Society for Testing and Materials, 1994, p. 437.
[17] P. Rudling, H. Pettersson, T. Andersson, T. Thorvaldsson, in: L.F.P. Van Swam, C.M. Eucken (Eds.), Zirconium in the Nuclear Industry: Eighth International Symposium, ASTM STP 1023, American Society for Testing and Materials, 1989, p. 213.
[18] H. Anada, K. Nomoto, Y. Shida, in: A.M. Garde, E.D. Bradley (Eds.), Zirconium in the Nuclear Industry: 10th International Symposium, ASTM STP 1245, American Society for Testing and Materials, 1994, p. 307.
[19] T. Andersson, T. Thorvaldsson, A. Wilson, A.M. Wardle, IAEA-SM-288/59, 1989, p. 435.
[20] J.P. Gros, J.F. Wadier, J. Nucl. Mater. 172 (1990) 85.
[21] Y.H. Jeong, Korean J. Mater. Res. 6 (6) (1996) 584.
[22] J. Liu, Z. Li, P. Li, M. Zhu, Q. Song, Proceedings of Asian Symposium on Zircaloy, Fukuoka, Japan, 13–14 May 1998.
[23] A.V. NiKulina, V.A. Markelov, M.M. Peregud, Y.K. Bibilashvili, V.A. Kotrekhov, A.F. Lositsky, N.V. Kuzmeko, Y.P. Shevnin, V.K. Shamardin, G.P. Nobylyansky, A.E. Novoselov, in: E.D. Bradley, G.P. Sabol (Eds.), Zirconium in the Nuclear Industry: 11th International Symposium, ASTM STP 1295, American Society for Testing and Materials, 1996, p. 785.
[24] G.P. Sabol, R.J. Comstock, R.A. Weiner, P. Larouere, R.N. Stanutz, in: A.M. Garde, E.D. Bradley (Eds.), Zirconium in the Nuclear Industry: 10th International Symposium, ASTM STP 1245, American Society for Testing and Materials, 1994, p. 724.
[25] S.-J. Kim, K.H. Kim, J.H. Baek, B.K. Choi, Y.H. Jeong, Y.H. Jung, J. Nucl. Mater. 256 (1998) 114.
[26] Y.H. Jeong, J.H. Baek, S.J. Kim, H.G. Kim, H. Ruhmann, J. Nucl. Mater. 270 (1999) 322.
[27] Y.H. Jeong, J.H. Baek, S.J. Kim, K.H. Kim, B.K. Choi, J.K. Bang, J. Korean Inst. Meth. Mater. 36 (7) (1998) 1138.
[28] B. Cox, AECL Rep. 9382, Atomic Energy of Canada Ltd., Chalk River Nuclear Laboratories, 1987.
[29] H.-J. Beie, A. Mitwalsky, F. Garzarolli, H. Ruhmann, H.-J. Sell, in: A.M. Garde, E.D. Bradley (Eds.), Zirconium in the Nuclear Industry: 10th International Symposium, ASTM STP 1245, American Society for Testing and Materials, 1994, p. 615.
[30] H. Anada, K. Takeda, in: E.D. Bradley, G.P. Sabol (Eds.), Zirconium in the Nuclear Industry: 11th International Symposium, ASTM STP 1295, American Society for Testing and Materials, 1996, p. 35.
[31] J. Godlewski, in: A.M. Garde, E.D. Bradley (Eds.), Zirconium in the Nuclear Industry: 10th International Symposium, ASTM STP 1245, American Society for Testing and Materials, 1994, p. 663.
[32] Ch. Valot, D. Ciosmark, M.T. Mesnier, M. Lallemant, Oxid. Met. 48 (3/4) (1997) 329.
[33] Y. Ding, D.O. Northwood, Corrosion Sci. 36 (2) (1994) 259.
[34] M.G. Glavicic, J.A. Szpunar, Y.P. Lin, J. Nucl. Mater. 245 (1997) 147.
[35] R. Hahn, J. Nucl. Mater. 245 (1997) 147.
[36] D. Pecheur, F. Lefebvre, A.T. Motta, C. Lemagnan, D. Charquet, in: A.M. Garde, E.D. Bradley (Eds.), Zirconium in the Nuclear Industry: 10th International Symposium, ASTM STP 1245, American Society for Testing and Materials, 1994, p. 687.